OPEN ACCESS



The Sun Remains Relatively Refractory Depleted: Elemental Abundances for 17,412 Gaia RVS Solar Analogs and 50 Planet Hosts

Rayna Rampalli ^{1,6} , Melissa K. Ness^{2,3,4} , Graham H. Edwards ^{1,5} , Elisabeth R. Newton ¹ , and Megan Bedell ⁴

Department of Physics and Astronomy, Dartmouth College, Hanover, NH 03755, USA; raynarampalli@gmail.com

Research School of Astronomy & Astrophysics, Australian National University, Canberra, ACT 2611, Australia

Department of Astronomy, Columbia University, 550 West 120th Street, New York, NY 10027, USA

Center for Computational Astrophysics, Flatiron Institute, 162 Fifth Avenue, New York, NY 10010, USA

Department of Earth Sciences, Dartmouth College, Hanover, NH 03755, USA

Received 2024 February 9; revised 2024 February 23; accepted 2024 February 23; published 2024 April 18

Abstract

The element abundances of stars, particularly the refractory elements (e.g., Fe, Si, and Mg), play an important role in connecting stars to their planets. Most Sun-like stars do not have refractory abundance measurements since obtaining a large sample of high-resolution spectra is difficult with oversubscribed observing resources. In this work we infer abundances for C, N, O, Na, Mn, Cr, Si, Fe, Ni, Mg, V, Ca, Ti, Al, and Y for solar analogs with Gaia Radial Velocity Spectrometer (RVS) spectra (R = 11,200) using TheCannon, a data-driven method. We train a linear model on a reference set of 34 stars observed by Gaia RVS with precise abundances measured from previous high-resolution spectroscopic efforts (R > 30,000-110,000). We then apply this model to several thousand Gaia RVS solar analogs. This yields abundances with average upper limit precisions of 0.04–0.1 dex for 17,412 stars, 50 of which are identified planet (candidate) hosts. We subsequently test the relative refractory depletion of these stars with increasing element condensation temperature compared to the Sun. The Sun remains refractory depleted compared to other Sun-like stars regardless of our current knowledge of the planets they host. This is inconsistent with theories of various types of planets locking up or sequestering refractories. Furthermore, we find no significant abundance differences between identified close-in giant planet hosts, giant planet hosts, and terrestrial/small planet hosts with the rest of the sample within our precision limits. This work demonstrates the utility of data-driven learning for future exoplanet composition and demographics studies.

Unified Astronomy Thesaurus concepts: Stellar abundances (1577); Solar system formation (1530); Solar abundances (1474)

Supporting material: machine-readable tables

1. Introduction

Know thy star, know thy planet: planets can reflect the chemical properties of their host star because they are formed from the same molecular cloud. Studying star-planet connections of other planetary systems using their host star chemistry can answer open questions we have about our own solar system. The Sun shows a trend of relative depletion in refractory elements (Na, Mn, Cr, Si, Fe, Ni, Mg, V, Ca, Ti, Al, and Y) with increasing condensation temperature compared to 80% of its Sun-like counterparts (Bedell et al. 2018), but the source of this relative depletion is unknown. Early work from Meléndez et al. (2009) and Ramírez et al. (2009) posit that the terrestrial planets have locked up these refractory elements. More recently, Booth & Owen (2020) suggested that giant planets (e.g., Jupiter) can create dust traps preventing the infall of refractory-rich dust onto the host star. In this work we aim to determine if this apparent refractory depletion is due to the planets in the solar system by comparing refractory abundances for solar analogs and identified solar-analog planet hosts.

Original content from this work may be used under the terms of the Creative Commons Attribution 4.0 licence. Any further distribution of this work must maintain attribution to the author(s) and the title of the work, journal citation and DOI.

When broadly considering the relationship between host star chemistries and their planets, there is a correlation between planet occurrence and host star iron abundance ([Fe/H] as a proxy for bulk metallicity) through exoplanet occurrence rate and demographics studies. Fischer & Valenti (2005) demonstrated that giant planets are more commonly found around high-metallicity stars, but there is a lack of consensus on whether the same relationship holds for smaller terrestrial planets (Buchhave et al. 2014; Petigura et al. 2018). Enhancement in abundances of individual elements generally increases with planet occurrence as well (Wilson et al. 2022).

Thus, precise abundances of planet hosts are a necessity to understand their planets' role in shaping their compositions and vice versa. Individual planet characterization efforts require observations from ground-based telescopes, and obtaining follow-up high-resolution spectroscopy for each system is difficult due to instrument oversubscription. Most Sun-like stars do not have precise abundance measurements, including for the refractory elements. This has limited opportunities to understand the connections between host star and planet chemical compositions on a demographic scale. However, the advent of large-scale spectroscopic and astrometric surveys of stars in our Galaxy and resulting data-driven methods complement planet characterization efforts quite well. The Gaia mission (Gaia Collaboration et al. 2016) alone has measured precise astrometry for over 1.4 billion stars. In its third data release (DR3; Gaia Collaboration et al. 2023), just under 1 million medium-resolution spectra were released with

⁶ NSF GRFP Fellow.

 $^{^{7}}$ We define an element as "refractory" if its 50% condensation temperature from Lodders (2003) > 900 K following Flores et al. (2024).

149 million more expected in the coming years from the Radial Velocity Spectrometer (RVS) instrument (Recio-Blanco et al. 2016).

To investigate whether the source of the Sun's refractory depletion is due to its status as a planet host, we infer abundances for several thousand solar analogs ($T_{\rm eff}$: $T_{\odot}\pm300\,\rm K$, $\log g$: $\log g_{\odot}\pm0.3$, and [Fe/H]: [Fe/H] $_{\odot}\pm0.3$ dex, as defined by Berke et al. 2023) observed by Gaia, a subset of which are identified planet hosts. We compile abundance information for solar analogs from archival high-resolution spectroscopic surveys that also have observed Gaia RVS spectra. We call this our reference set. We then train a linear model with TheCannon (Ness et al. 2015) on these spectra and abundances, apply it to other Gaia stars (our test set) to infer precise abundances, and examine refractory depletion trends with respect to the Sun and between planet host populations.

In Section 2, we discuss the literature solar analogs used to make up our reference set, the Gaia RVS spectra used to make up our test set, and the planet host catalogs we crossmatch with our test set of stars. We outline what TheCannon is, how it is used to test the robustness of the reference set and the model, how it is applied to the test set, and how we inferred isochrone ages for the test set in Section 3. In Section 4, we show TheCannon results and the resulting refractory depletion trends with the test set. We also show the precision limits that the Gaia RVS spectra allow. We conclude with a discussion of our results in Section 5.

2. Data

2.1. Literature Solar Analogs

To build our reference set sample of stars, we search the literature for solar analogs (T_{\odot} : 5772 \pm 300 K, $\log g_{\odot}$: 4.44 \pm 0.3, and [Fe/H] $_{\odot}$: 0.0 \pm 0.3 dex as defined by Prša et al. 2016) with \geqslant 10 precise abundances measured from high-resolution spectra. We find 1294 unique stars from the Bensby et al. (2014), Hinkel et al. (2014), Brewer et al. (2016), Brewer & Fischer (2018), and Bedell et al. (2018) catalogs with abundance measurements for C, N, O, Na, Mn, Cr, Si, Ni, Mg, V, Ca, Ti, Al, and Y.

Bensby et al. (2014) conducted a high-resolution (R =40,000–110,000) spectroscopic survey of 714 F and G dwarf and subgiant stars in the solar neighborhood. This was done using the FEROS spectrograph on the ESO 1.5 m and 2.2 m telescopes, the SOFIN and FIES spectrographs on the Nordic Optical Telescope, the UVES spectrograph on the ESO Very Large Telescope, the HARPS spectrograph on the ESO 3.6 m telescope, and the MIKE spectrograph on the Magellan Clay telescope. Average errors are 56 K for $T_{\rm eff}$, 0.08 dex for $\log g$, and <0.1 dex for [X/Fe], which we convert to [X/H]. Hinkel et al. (2014) compiled spectroscopic abundance data from 84 literature sources for 50 elements across 3058 stars in the solar neighborhood, within 150 pc of the Sun. The different instruments used are more than we can feasibly list here, but the minimum resolution reported starts at R = 30,000. Average errors are 100 K for $T_{\rm eff}$ and 0.03-0.1 dex for [X/H]. Brewer et al. (2016) and Brewer & Fischer (2018) performed a uniform spectroscopic analysis ~2700 F, G, and K dwarfs through the California Kepler Survey with Keck HIRES (R = 70,000). Average errors are 27 K for T_{eff} , 0.05 dex for $\log g$, and <0.1 dex for [X/H]. Bedell et al. (2018) conducted a spectroscopic study and measured 30 elemental abundances for 79 Sun-like stars within 100 pc using the HARPS spectrograph (R = 115,000) on the 3.6 m telescope of ESO. These stars had the smallest average errors with 4 K for $T_{\rm eff}$, 0.01 dex for $\log g$, and <0.02 dex for [X/H].

We use the respective catalog ID names and crossmatch them to Gaia stars using the Gaia Archive with a 2" radius. Of these 1294 stars, only 105 had observed Gaia RVS spectra available in Gaia DR3 (11 from Bensby et al. 2014; 11 from Hinkel et al. 2014; 78 from Brewer et al. 2016; Brewer & Fischer 2018; and five stars from Bedell et al. 2018). Upon examining the RVS spectra of the literature stars individually, we find a handful of spectra that deviate from a typical Sun-like spectrum such as magnetically induced active stars showing emission at the Ca triplet (Martin et al. 2017). Because we are interested in finding solar analogs, we want to exclude such outliers from our eventual reference set. We construct a "median solar-analog spectrum" by choosing the median RVS flux value at each wavelength step across the entire literature sample. The median solar-analog spectrum is then compared to each individual literature star's spectrum using two χ^2 tests. The spectra here extend from 846.4 to 869.6 nm in steps of 0.01 nm, yielding 2321 wavelength steps. We compare across (i) the entire spectrum and (ii) at the calcium triplet lines as this is where the most variance is usually found (Rampalli et al. 2021). We define a reasonable 8 χ^2 as $\leqslant 2$ times the degrees of freedom, which corresponds to (i) the number of wavelength steps making up the entire spectrum (2321) and (ii) the number of wavelength steps containing the calcium triplet lines (69). We remove the stars that do not meet this χ^2 threshold. We then reconstruct the median solar analog with the updated set of stars and repeat the χ^2 comparison. In this second iteration, we do not find any stars that have an unreasonably high χ^2 . We are left with 96 stars, and these are the stars that make up our reference set. None of the spectroscopic outliers we remove have unique abundance patterns that deviate from the abundance distributions of our finalized reference set.

While four catalogs have measurements for C, N, Mn, and V, that of Bensby et al. (2014) does not. For our analysis with TheCannon, we initially take the mean of the other catalogs' measurements for each of these elements and use these mean values for the Bensby et al. (2014) stars. We do the same for the Bedell et al. (2018) catalog, which did not report abundances for N. Ultimately, we choose to exclude stars from Bensby et al. (2014) to improve our inferred abundance precision. We describe this decision further in Section 3.1.1. This decreases our reference set from 96 stars to 85 stars though we do not make this cut until we use TheCannon to infer abundances. We still include the Bensby et al. (2014) stars when deciding what our test set of stars will be.

We show the reference set's distributions of $T_{\rm eff}$, $\log g$, and elements Fe, Mg, C, N, O, Na, Mn, Cr, Si, Ni, V, Ca, Ti, Al, and Y with respect to H in Figure 1. The Brewer et al. (2016) and Brewer & Fischer (2018) stars are light blue and labeled as Br16 and Br18, respectively, the Hinkel et al. (2014) stars are orange and labeled as H14, and the Bedell et al. (2018) stars labeled as B18 are pink. The distributions of stars from each catalog are wide in comparison to those from Bedell et al. (2018) since the latter specifically targeted solar twins. We

 $^{^8}$ A χ^2 < the number of degrees of freedom indicates the data are being overfitted, and a χ^2 > 3–5 times the number of degrees of freedom indicates the data are not being fit well. We choose two to be conservative.

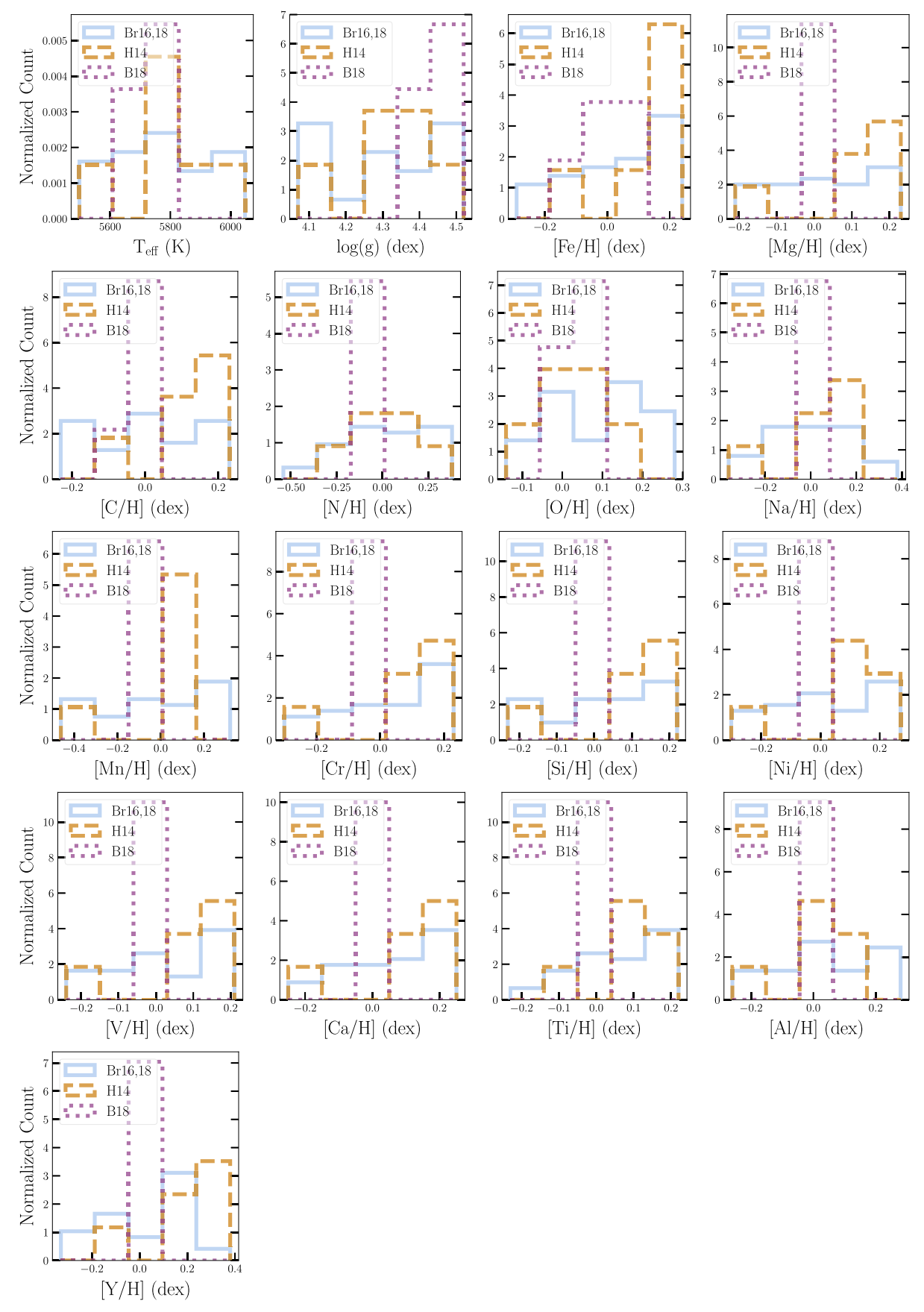


Figure 1. Distributions of $T_{\rm eff}$, $\log g$, Fe, Mg, C, N, O, Na, Mn, Cr, Si, Ni, V, Ca, Ti, Al, and Y with respect to H for the reference set. Brewer et al. (2016) and Brewer & Fischer (2018) are labeled as Br16 and Br18 in light blue, Hinkel et al. (2014) is denoted H14 in orange, and Bedell et al. (2018) is given as B18 in pink.

Table 1
Reference Set Parameters

Column	Format	Units	Example	Description	
Identifier:					
DR3id	integer	•••	746545172372256384	Gaia DR3 ID	
Coordinates:					
ra	float	degrees	150.249968	R.A.	
dec	float	degrees	31.921762	Decl.	
Literature Values:					
teff	integer	K	5742	$T_{\rm eff}$ measurement	
logg	float	dex	4.31	$\log g$ measurement	
Fe_H_	float	dex	0.2	[Fe/H] measurement	
Mg_H_	float	dex	0.21	[Mg/H] measurement	
C_H_	float	dex	0.15	[C/H] measurement	
N_H_	float	dex	0.13	[N/H] measurement	
O_H_	float	dex	0.18	[O/H] measurement	
Na_H_	float	dex	0.23	[Na/H] measurement	
Mn_H_	float	dex	0.23	[Mn/H] measurement	
Cr_H_	float	dex	0.2	[Cr/H] measurement	
Si_H_	float	dex	0.2	[Si/H] measurement	
Ni_H_	float	dex	0.24	[Ni/H] measurement	
V_H_	float	dex	0.2	[V/H] measurement	
Ca_H_	float	dex	0.23	[Ca/H] measurement	
Ti_H_	float	dex	0.19	[Ti/H] measurement	
Al_H_	float	dex	0.24	[Al/H] measurement	
Y_H_	float	dex	0.2	[Y/H] measurement	
prov	string		brewer	Catalog author	
Gaia RVS Parameters:	-			-	
snr	integer	•••	1301	S/N of the star's RVS spectrum	
teff_gspspec	integer	K	5730	Measured $T_{\rm eff}$ from Gaia RVS	
logg_gspspec	float	dex	4.06	Measured log g from Gaia RVS	
feh_gspspec	float	dex	0.09	Measured [Fe/H] from Gaia RVS	

Note. The complete table is available in the online journal and as a CSV with the arXiv submission. (This table is available in its entirety in machine-readable form.)

show the stars' Gaia DR3 names, their coordinates, literature measurements, the signal-to-noise ratio (S/N) of their Gaia RVS spectra, and a selection of the parameters measured from the RVS spectra in Table 1.

2.2. Gaia RVS Spectra

Launched in 2013, the Gaia space telescope has created the largest and most precise 3D kinematic catalog of objects in the sky. Gaia is equipped with an astrometry instrument (ASTRO), which measures positions and the photometric instrument (BP and RP filters), which measures fluxes. Its third instrument, the RVS, measures line-of-sight velocities and is expected to obtain >150 million spectra in the Ca triplet region (845–870 nm) at a resolution of R = 11,200 (Recio-Blanco et al. 2016). With repeat observations, the S/N will improve as these are combined (Cropper et al. 2018). The third and latest data release, DR3 (Gaia Collaboration et al. 2023), provides full astrometric solutions for over 1.46 billion stars in the Galaxy. DR3 also includes spectra for just under one million stars from RVS and stellar parameters from RVS spectra including $T_{\rm eff}$, $\log g$, [Fe/H], and $[\alpha/{\rm Fe}]$ and abundances for 13 elements: N, Mg, Si, S, Ca, Ti, Cr, Fe I, Fe II, Ni, Zr, Ce, and Nd (Recio-Blanco et al. 2023).

We are ultimately interested in finding solar analogs in the Gaia RVS spectra sample. Rather than examining all 999,645 spectra, we choose a 3D box in $T_{\rm eff}$, $\log g$, and [Fe/H] space centered around the mean Gaia RVS reported $T_{\rm eff}$, $\log g$, and [Fe/H] of the reference set (see Table 1). This way the values are

homogenized in Gaia across the catalogs from the literature. We select the box to extend 3–5 σ from the mean of the values for the reference set, which includes all of the reference stars. The box is defined such that $T_{\rm eff}$: 5804 ± 868 K, $\log g$: 4.085 ± 1.27 dex, and [Fe/H]: -0.11 ± 0.57 dex, and it contains 75,545 stars. We do a χ^2 comparison with the median solar-analog RVS spectrum constructed from the reference set and all 75,545 stars from the 3D box in parameter. Using the same χ^2 thresholds when updating the reference set leaves 64,557 stars with Gaia RVS spectra that make up our eventual test set.

We also remove the first and last wavelength steps (4 nm) from each RVS spectrum as there are often spurious flux values in these regions. This makes up 3% of the spectrum and does not affect the subsequent analyses.

2.3. Planet Host Catalogs

Our interest in solar-analog planet hosts arises from the the Sun and its status as a planet host. We start by crossmatching the 64,557 Gaia RVS stars to the 7993 planet (candidate) hosts and corresponding stellar and planet parameters from Berger et al. (2023) by Gaia DR3 ID. This catalog is more expansive than the exoplanet archive as it includes \sim 4000 planet candidates in addition to \sim 5000 confirmed planets. It reports homogenized and precise stellar and planet parameters that were derived using Gaia DR3 photometry, parallaxes, spectrophotometric metallicities, and isochrone fitting (Huber et al. 2017; Berger et al. 2020). We follow this with a crossmatch by

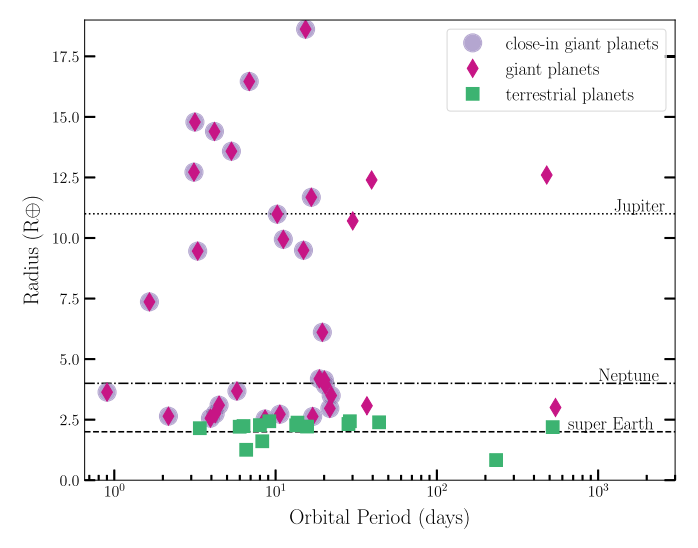


Figure 2. Distribution of planets hosted by postanalysis Gaia RVS test set stars in orbital period–radius space. Super-Earth, Neptune, and Jupiter radii are demarcated by dashed, dashed–dotted, and dotted lines, respectively. We classify planets as close-in giant planets (>2.5 R_{\oplus} , <30 day orbital period) shown as purple circles, giant planet hosts (>2.5 R_{\oplus}) shown as pink diamonds, and "terrestrial"/small planets (<2.5 R_{\oplus}) as green squares.

Gaia ID to the Exoplanet Archive (NASA Exoplanet Archive 2023) to catch any planet systems not in the Berger et al. (2023) catalog. In Figure 2, we show the 61 planets hosted by 50 of our test set stars in orbital period–radius space that we categorize as close-in giant planets, giant planets, and terrestrial/small planets in Section 4.2.

3. Methods

3.1. Applying TheCannon

We use TheCannon (Ness et al. 2015) implementation from Ho et al. (2017) to infer increased-precision stellar parameters and abundances for solar analogs identified with the Gaia RVS spectra. TheCannon is a data-driven method that can cross-calibrate between surveys and has been used successfully many times across various surveys (e.g., Casey et al. 2017; Wheeler et al. 2020; Wylie et al. 2021; Walsen et al. 2024). TheCannon builds a model to describe the variability in spectra using a set of reference stars (called the reference set) with known and precise stellar parameters and abundances such as $T_{\rm eff}$, $\log g$, [Fe/H], $[\alpha/{\rm Fe}]$, and [X/H], which we more generally call "labels" following machine-learning terminology. The model is then applied to a test set of stars with unknown or imprecise existing labels in the same survey.

A linear⁹ or more often a polynomial model has been typically used with TheCannon to connect the reference stars' labels to their spectra in the training step. If, for example, we chose a linear model made up of four labels $T_{\rm eff}$, $\log g$, [Fe/H], and $[\alpha/{\rm Fe}]$ for star n, each flux value for this star, F_n , in the star's spectrum with a number of wavelength steps, λ , would be represented as the following equation for training the model, for a set of n reference objects:

$$F_{n_{\lambda}} = A_{\lambda}(T_{\text{eff}n}) + B_{\lambda}(\log g_n) + C_{\lambda}([\text{Fe/H}]_n) + D_{\lambda}([\alpha/\text{Fe}]_n) + E_{\lambda} + \sigma_{\lambda}.$$
(1)

 $T_{\mathrm{eff}\,n}$, $\log g_n$, $[\mathrm{Fe/H}]_n$, and $[\alpha/\mathrm{Fe}]_n$ are the labels for the nth star in the reference set vector, more generally represented as the label matrix, l_n . A_{λ} , B_{λ} , C_{λ} , D_{λ} , and E_{λ} are the coefficients for which TheCannon solves and are more generally represented by the coefficient matrix, θ_{λ} . σ_{λ} is the noise term and is the rms sum of the observational error on each flux value $(\sigma_{n,\lambda})$ and the scatter in the model at each wavelength (s_{λ}) .

During TheCannon's training step, Equation (1) is rerepresented as a single-wavelength step log-likelihood function that is optimized to solve for θ_{λ} and s_{λ} using the input l_n and the input flux and uncertainty for the n reference objects. Then, to infer the label matrix for the test set of m stars, l_m , the same log-likelihood is optimized, but θ_{λ} and s_{λ} are held constant instead. Additionally, the optimization is done as a least-squares fit over the whole spectrum rather than per wavelength step.

We build a reference set of 85 solar-analog labels measured in high-resolution (R > 30,000) spectroscopic surveys as described in Section 2.1. We identify the reference stars associated with high-S/N Gaia RVS spectra and train a 17-label linear model ($T_{\rm eff}$, log g, [Fe/H], [Mg/H], [C/H], [N/H], [O/H], [Na/H], [Mn/H], [Cr/H], [Si/H], [Ni/H], [V/H], [Ca/H], [Ti/H], [Al/H], and [Y/H]) on the high-precision labels and Gaia RVS spectra with TheCannon. We then use this model to infer labels for 64,557 spectroscopically similar Gaia RVS stars (as determined and described in Section 2.2).

3.1.1. Testing the Validity of the Reference Set

In order to apply TheCannon to our test set of >60,000 stars, it is important to ascertain that the reference set and associated model are robust. We employ a cross-validation test after the training time and prior to the test time, where we iteratively treat each star in the reference set as a "test star." For a given test star, we remove its spectrum and labels from the reference set, and TheCannon trains on the rest of the reference set to predict the test star's labels and spectrum. We run this procedure for every star. In turn, we are able to evaluate, for each label in the reference set ($T_{\rm eff}$, $\log g$, [Fe/H], [Mg/H], [C/H], [N/H], [O/H], [Na/H], [Mn/H], [Cr/H], [Si/H], [Ni/H], [V/H], [Ca/H], [Ti/H], [Al/H], and [Y/H]), how well the model's inferred values match the reference set values from the literature.

For a single label, if the 1σ standard deviation of the ensemble's <code>TheCannon-predicted</code> values – the literature values, or (σ_{cval}) is less than the 1σ standard deviation across the literature values in the reference set (σ_{lit}) , this shows the model learned this particular label. If $\sigma_{cval} \geqslant \sigma_{lit}$, this means the model is doing no better than randomly drawing from the reference label distribution. For example, for the <code>[Fe/H]</code> label, the 1σ standard deviation in the literature values is 0.14 dex. <code>TheCannon</code> can predict the literature <code>[Fe/H]</code> to an average precision of $\sigma_{cval} = 0.04$ dex, which is much smaller than the 1σ standard deviation of the reference set <code>[Fe/H]</code> values, indicating <code>TheCannon</code> model is learning the label of <code>[Fe/H]</code> from the spectra.

The Cannon requires a reference set with a high S/N. We find that a S/N \geqslant 50 (45 stars) is sufficient in that the standard deviation of the predicted – literature values is generally less than the standard deviation of the literature values for each label. We find improved precision with a S/N \geqslant 100 (34 stars) and adopt this limit. With any higher S/N, we have too few

⁹ Because of the restricted parameter space, we find a linear model is sufficient to describe the data (which is often the case, e.g., Hogg et al. 2019; Birky et al. 2020) and that the polynomial model overfits the data.

stars to build a reliable model because the number of stars reaches the number of coefficients in the model. The cross-validation test with these 34 stars results in a standard deviation of 55 K in $T_{\rm eff}$, 0.08 dex in $\log g$, 0.036 dex in [Fe/H], 0.042 dex in [Mg/H], 0.051 dex in [C/H], 0.119 dex in [N/H], 0.067 dex in [O/H], 0.076 dex in [Na/H], 0.089 dex in [Mn/H], 0.04 dex in [Cr/H], 0.032 dex in [Si/H], 0.036 dex in [Ni/H], 0.053 dex in [V/H], 0.045 dex in [Ca/H], 0.036 dex in [Ti/H], 0.05 dex in [Al/H], and 0.066 dex in [Y/H]. We show the literature values versus TheCannon values with a 1:1 line, the 1σ standard deviation of predicted values from TheCannon—the literature values $(\sigma_{\rm cval})$, the mean error on the label from the literature $(\overline{\sigma_{\rm lit}})$, and the bias (or the mean difference in predicted and literature values, $\overline{\Delta}$) in Figure 3.

We see [N/H] has the highest standard deviation, and that there is a pileup of stars at a single literature value of [N/H] in Figure 3 (second row and second panel). These are the stars from Bedell et al. (2018) that did not have reported abundances for N. As discussed in Section 2.1, for reference stars that did not have certain labels, we assign them the mean of the population as TheCannon does not formally handle partial labels. This means that these stars are "badly labeled," which in turn yields poorer cross-validation results (e.g., a higher standard deviation) for N. In previous iterations, we included the stars from Bensby et al. (2014) which did not have measurements for four abundances and also made up one-quarter of the reference set. This yielded poor crossvalidation results that also affected the subsequent analyses, so we exclude them from our reference set when using TheCannon.

We compare $\sigma_{\rm cval}$ (as pink circles) with $\sigma_{\rm lit}$ (as gray squares) for each label; this is summarized in Figure 4. No $\sigma_{\rm cval}$ for any label exceeds $\sigma_{\rm lit}$. With the newly inferred labels, TheCannon can also generate model spectra to compare to the observed spectra. We show an example TheCannon-generated model spectrum as the blue dashed line and the RVS spectrum in pink for a reference star in the top panel of Figure 5. The residuals are plotted in black in the bottom panel and are on the scale of 0.5% or less, indicating the model is working very well. The maximum of each reference star's residuals found in the reference set are on average $1.5\% \pm 0.9\%$.

3.1.2. Inferring Labels for the Test Set

Given the robust performance of the model during crossvalidation, we train the model on the entire high-S/N reference set (34 stars) and apply TheCannon model to our test set of 64,557 stars. For each set of labels for each star, we have an associated error that is the rms sum of σ_{cval} and the unique noise term, σ_{λ} , returned in the star's covariance matrix. We use the labels and associated errors to generate a model spectrum and calculate a χ^2 goodness of fit for each star. We remove any stars with a $\chi^2 > 4642$, which is 2 times the number of degrees of freedom, or the number of wavelength steps in the spectrum ($\lambda = 2321$). We are left with 63,725 stars. The Cannon can extrapolate in label inference beyond the domain of values set by the range of the reference set labels. To keep our results robust, we remove anything outside of the reference set labels and are left with 17,412 stars. This drop is mainly attributed to stars being too hot or too cold compared to the temperature

range of the reference set. As mentioned in Section 2.3, 43 of these stars have been identified as planet (candidate) hosts.

3.2. Inferring Isochrone Ages from the Test Labels

Since the reference set does not have precise reported ages, we do not include age in our model. However, we are interested in exploring the effects of age in our work. We recognize that because these are main-sequence field stars, the ages inferred using stellar models will be imprecise. We fit isochrones to each star and coarsely estimate ages that we use as points of exploration. We do not report these as robust results for individual stars. However they serve as a measure of the overall population age distribution.

We infer ages for our test set with isoclassify (Huber et al. 2017; Berger et al. 2020). isoclassify uses an isochrone grid modeling approach. Isochrones from the MIST database (Paxton et al. 2011, 2013, 2015; Choi et al. 2016; Dotter 2016) are interpolated and used to calculate a grid of ages from 0.5 to 14 Gyr (step size of 0.25 Gyr) and metallicities from -2 to 0.4 dex (step size of 0.02 dex). Given observables, isoclassify calculates priors and likelihoods and integrates over all points in the grid to derive posterior distributions following Serenelli et al. (2017).

For simplicity, we only use the spectroscopic properties, $T_{\rm eff}$, $\log g$, and [Fe/H] inferred from TheCannon, as these are intrinsic properties to the star. We do not account for reddening as 90% of our stars have $A_V < 0.2$ from the calculated reddening in the Gaia bandpasses using <code>Bayestarl9</code> (Green et al. 2019), so these properties inferred from the spectra should not be affected. We find that these stars are on average 5.8 ± 2.3 Gyr, and we show the distribution of ages in Figure 6. The average age error across the test set is 1.84 ± 0.77 Gyr.

4. Results

We successfully infer labels for 17,412 stars. These stars have inferred labels that are within the label range of our reference set and a reasonable χ^2 fit (discussed in Section 3.1.2) between the RVS spectra and TheCannon-generated models. We include a table of the 17 labels and label errors inferred with TheCannon, age and age errors from isoclassify, and planet host status in Table 2. The average error value on each label is 61 K for $T_{\rm eff}$, 0.09 dex for $\log g$, and 0.04–0.1 dex for [X/H].

We subtract the model spectra generated with the stars' labels from the observed RVS spectra and show the residual flux vectors of our test set in Figure 7 arranged from lowest (bottom) to highest S/N (top). The residuals look fairly stochastic with marginally higher residuals for high-S/N stars but still typically subpercent amplitudes. On average, we find residuals of $0.04\% \pm 0.03\%$.

Of note are the Ca triplet lines, which have residuals of near zero, indicating that the model performs very well. This is a slight departure from Rampalli et al. (2021), where the strongest residuals were seen for the Ca lines. The cores of the Ca lines are formed in the stellar chromosphere (e.g., Andretta et al. 2005). These cannot be properly modeled under the typical one-dimensional, local thermal equilibrium assumption invoked when deriving stellar parameters (Magic et al. 2013). An important difference between our prior work and this work is that here we restrict our study to a much

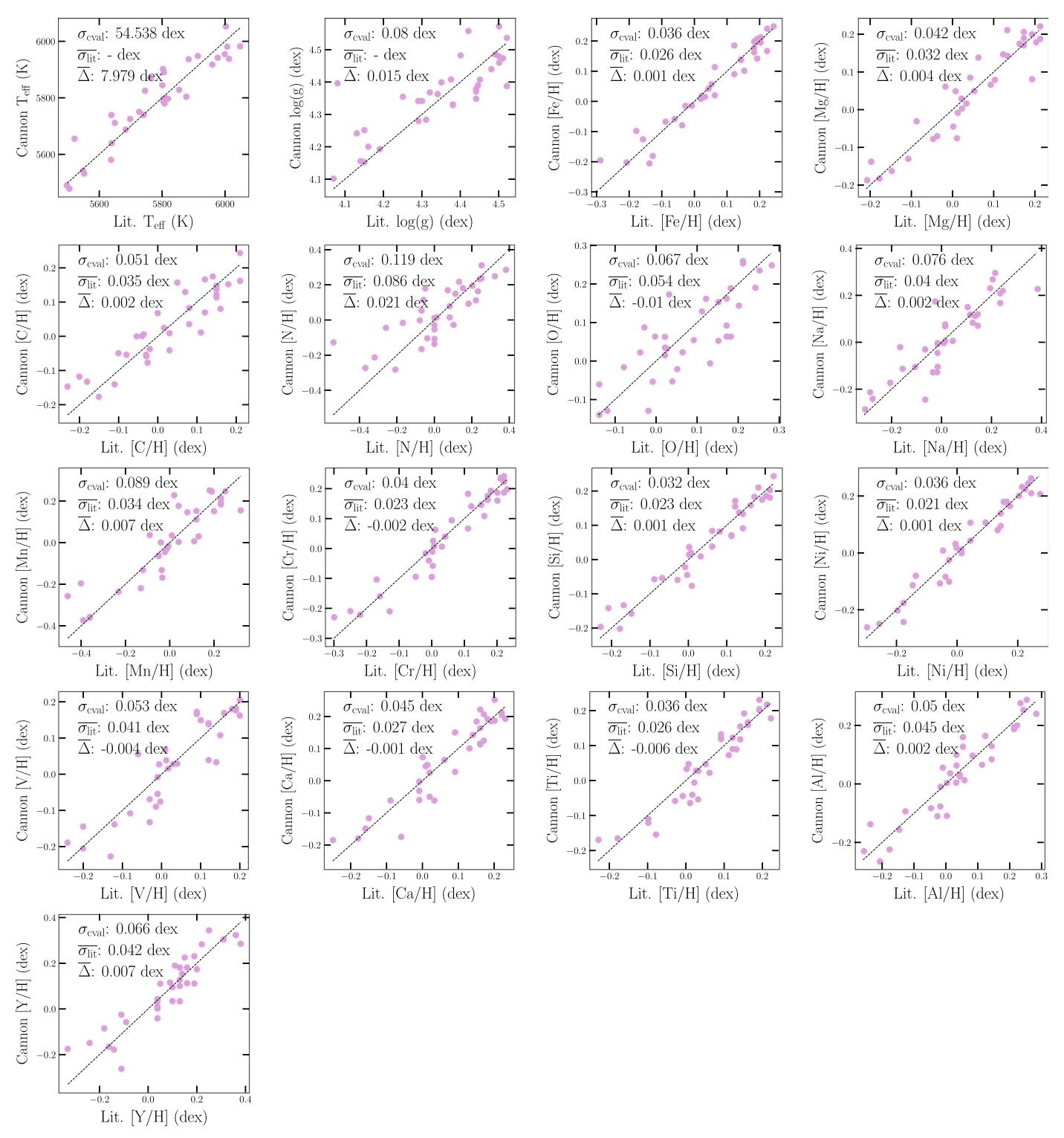


Figure 3. Literature label values vs. TheCannon model-predicted label values with the 1:1 ratio shown as a black dashed line, the 1σ standard deviation of predicted values from TheCannon – literature values (σ_{cval}), the mean error on the label from the literature ($\overline{\sigma_{lit}}$), and the bias (or the mean difference in predicted and literature values, $\overline{\Delta}$). $\overline{\sigma_{lit}}$ was not available for T_{eff} and $\log g$ as these were not reported for stars from Hinkel et al. (2014).

smaller parameter space that describes solar analogs, and we see that the linear model can well describe the flux given the labels. In Rampalli et al. (2021), we covered a broader range of $\log g$ from two to three using a second-order polynomial model to describe red clump stellar spectra. The Ca line residuals found there were already small at the percentage level. Therefore, it is not surprising these residuals decrease

significantly in our work and are not necessarily at odds with previous results.

We show the coefficients of the model for each label in Figure A1 of the Appendix. This shows at what wavelengths the model is learning from for each label. We see that most have the highest amplitudes at the cores and wings of the Ca lines, similar to Rampalli et al. (2021). While there are shared

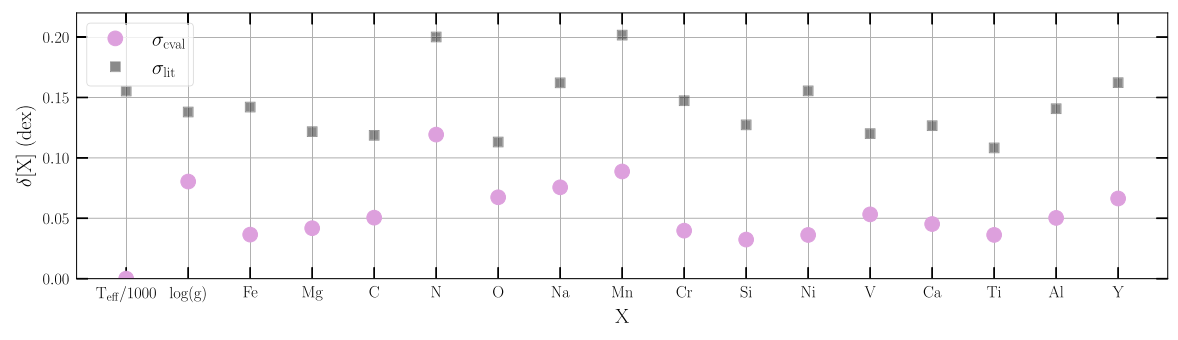


Figure 4. Summary of cross-validation results for each label. Standard deviation (1σ) of predicted values from TheCannon – literature values (σ_{cval}) are plotted as pink circles. The standard deviations (1σ) of the reference set's literature values (σ_{int}) are plotted as gray squares.

regions of the spectra that the model learns from for each label, the coefficient shapes are in detail different.

4.1. The Dimensionality and Precision Limits of Gaia RVS Spectra

In large-scale and low- to medium-resolution spectroscopic surveys, the concept of dimensionality has been explored at great length (e.g., Ting et al. 2012; Price-Jones & Bovy 2018; Griffith et al. 2021; Ting & Weinberg 2022): how many necessary labels are needed to describe the variance seen in the spectra and the chemical abundance measurements derived from these spectra? We explore the dimensionality of Gaia RVS spectra by seeing how well the four fundamental labels, $T_{\rm eff}$, $\log g$, [Fe/H], and [Mg/Fe] (with [Mg/H] – [Fe/H] representing alpha enrichment, $[\alpha/Fe]$) inferred from TheCannon and ages from isoclassify can predict the other 13 abundances inferred from TheCannon. If we can perfectly predict the 13 abundances within their errors from these five labels, this indicates the data are low dimensional and that the labels are all entirely correlated. This means that we are not gleaning any new information from the elemental abundances that is not already reported in the T_{eff} , $\log g$, [Fe/H], [Mg/Fe], and age measurements. The measurement precision that can be reached by a spectroscopic survey increases with instrument resolution. Prior work in this realm indicates that very high-resolution, highfidelity data (e.g., from the HARPS spectrograph; Mayor et al. 2003) are required to access the information in stellar spectra beyond that captured in a few labels (e.g., Ness et al. 2022).

Following the methodology outlined in Section 3.1, we implement a linear regression with Python's sklearn to predict element abundances using the five fundamental labels of T_{eff} , $\log g$, [Fe/H], [Mg/Fe], and age. Equation (1) is invoked again but instead of having the labels and coefficients describe a vector of flux values, the vector is substituted with a single abundance value. We find that all 13 element labels from TheCannon are predicted with the five-label regression to within the errors. This is consistent with results using other similar-resolution surveys such as ARGOS and RAVE (Casey et al. 2017; Rampalli et al. 2021). Griffith et al. (2021) show that even with higher-resolution surveys like APOGEE (R = 22,500), a subset of elements, [Mg/Fe] and [Mg/H], is all that is needed to predict other abundances. We test this by using a linear regression model with only [Mg/Fe] and [Mg/H] and subsequently [Fe/H] and [Mg/Fe] and find that in both cases indeed two labels are enough to predict the other abundances within their errors.

It is important to note that the errors reported here, though dominated by the cross-validation term, $\sigma_{\rm cval}$, are upper limit

errors. This is because the errors in the reference labels are folded into these numbers (Manea et al. 2023). We can measure the intrinsic dispersion, $\sigma_{\rm int}$ to assess better TheCannon's performance and Gaia RVS. σ_{int} is the difference of σ_{cval} and the mean error (σ_{int}) in quadrature for each label. We calculate a $\sigma_{\rm int}$ of 0.02 dex for Si and Al all the way to 0.08 dex for N due to bad input labels as discussed in Section 3.1.1. We report $\sigma_{\rm int}$ for all of the abundances in Table 3. If we consider the twolabel model regression results using intrinsic dispersions rather than our reported errors, we still find that we can 100% predict 7/13 abundances. There are six exceptions: C (97%), N (94%), O (87%), Ti (98%), Al (92%), and Y (98%). Thus, even when considering reference label errors, we still find the abundance data are low dimensional, consistent with previous studies (Casey et al. 2017; Griffith et al. 2021; Rampalli et al. 2021). Obtaining intrinsic abundance information, beyond the 2-5 labels, can only be accessed if the abundance precision is higher than the intrinsic dispersion measurements for these abundances (<0.02 dex), as also found in Behmard et al. (2023). In spite of the low precision on individual measurements, we are able to test for potential planet host differences in the amplitudes of the element abundances, in particular with condensation temperature, given the size of our data set, as demonstrated in the next section. Because the planet sample is a small portion of the test set, differences in individual abundances as a function of planet status could be present at a level lower than our overall precision.

4.2. Planet Host Comparisons

Of the 17,412 stars in our test set, 50 are known planet (candidate) hosts, as shown in Figure 2. The 61 planets span a range of radii and orbital periods. We list the planet parameters and host star information in Table 4. For our analysis, we further categorize the sample of planet hosts into the 27 stars hosting close-in giant planets ($R_{\oplus} > 2.5$, orbital period < 30 days), the 35 stars hosting giant planets (>2.5 R_{\oplus}), and the 15 stars that lack known close-in or distant giant planets and host "terrestrial" or small planets ($<2.5~R_{\oplus}$). The $R=2.5~R_{\oplus}$ boundary is chosen to have the closest radius value to terrestrial-sized planet radii (typically $\leq 2 R_{\oplus}$) that still maintains a statistically substantial population of stars. We recognize that the delineation between "terrestrial" planets and giant planets is somewhat arbitrarily drawn. We conduct the following comparison tests using cuts of 3, 4, and 5 R_{\oplus} and ultimately find the same results. We also call stars in the test set without identified planets nonplanet hosts, though we recognize it is highly likely that many of these stars host as-yet-undetected planets since 50%-70% of Sun-like stars host planets (Mulders et al. 2018; Zink et al. 2019).

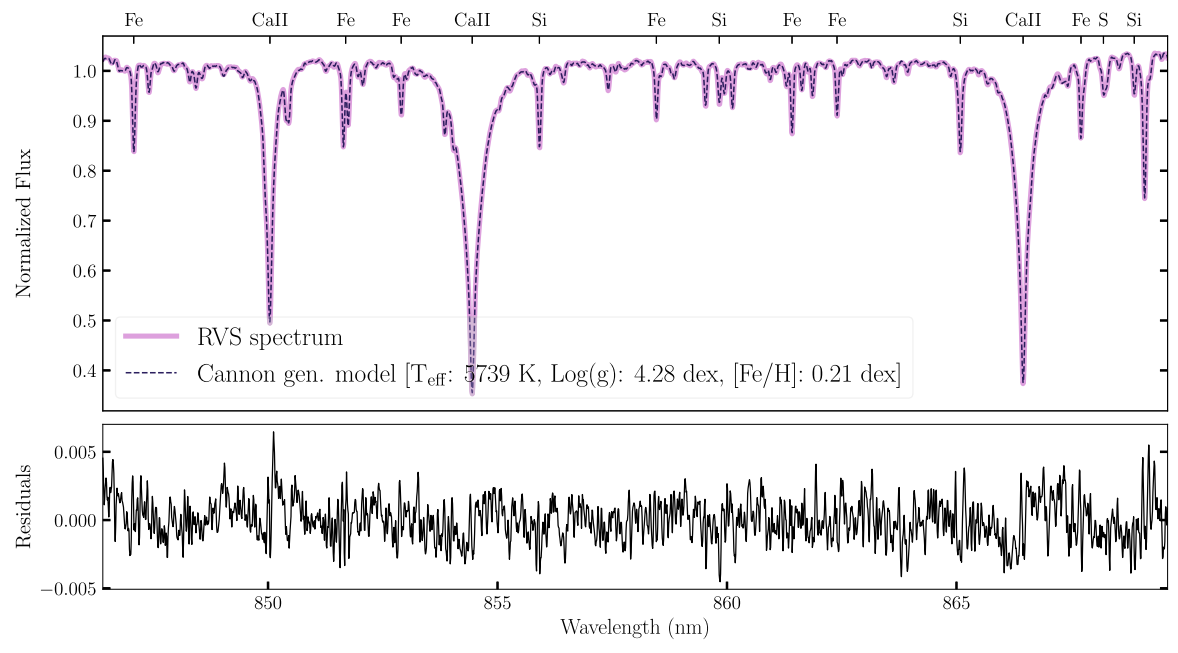


Figure 5. Top: example RVS spectrum from the reference set (pink) with generated model spectrum (blue dashed line) from TheCannon cross-validation and inferred labels of $T_{\rm eff} = 5739$ K, $\log g = 4.28$ dex, and $[{\rm Fe/H}] = 0.21$ dex. Bottom: residuals of data – model in black, which are on the order of 0.5%.

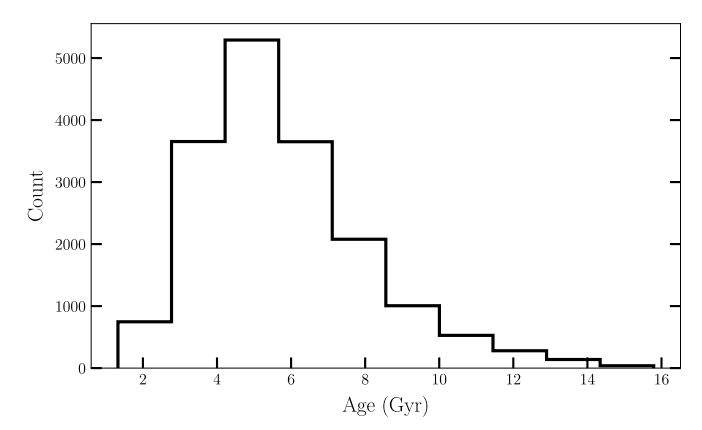


Figure 6. Approximate age distribution of the test set using $T_{\rm eff}$, $\log g$, and [Fe/H] as input to isoclassify. Stars are on average $5.8 \pm 2.3~(1\sigma)$ Gyr.

4.2.1. Refractory Depletion Trends for the Sun

While measuring precise abundances for planet hosts has many applications, we examine the abundance space of solar-analog planet hosts compared to the Sun. The Sun has long thought to be refractory depleted compared to other Sun-like stars. Bedell et al. (2018) confirmed this with an extensive high-resolution spectroscopic survey of solar twins, 80% of which were refractory enriched with increasing condensation temperature compared to the Sun. Abundance comparison efforts of solar-analog planet hosts and the Sun suggested that the missing refractories are trapped by the terrestrial planets (Meléndez et al. 2009; Ramírez et al. 2009), or the giant planets created dust traps thereby keeping refractories from the host star (Booth & Owen 2020). If either of these theories were true, we would expect to find that planet hosts with terrestrial planets or giant planets have the same abundances as the Sun.

In Figure 8 we show the mean abundances and report the confidence on the mean with the error bars (as calculated by the standard deviation divided by the square root of the number of

stars) compared to the Sun as a function of condensation temperature for our entire test set, all planet hosts, close-in giant planet hosts, giant planet hosts, and terrestrial planet hosts. The condensation temperatures used are the 50% condensation temperatures calculated for solar-system-composition gas from Lodders (2003). We examine the trend of refractory depletion with increasing condensation temperature starting with Na (958 K) to Y (1658 K). We also convert all of our abundances from [X/H] to [X/Fe] so our results are analogous to those of Bedell et al. (2018).

The entire test set does not significantly differ from any kind of planet host by more than 3σ . In most cases, they are chemically indistinguishable within $1-2\sigma$. We also see that all four populations are largely refractory enriched compared to the Sun, replicating the finding of Bedell et al. (2018). We show the results of fitting a line to each of these populations for just the refractory elements (Na, Mn, Cr, Si, Ni, Mg, V, Ca, Ti, Al, and Y) in Figure 9. Visually, it appears that the slope for all of the test set stars $(-1.1 \pm 0.4 \times 10^{-4} \text{ dex K}^{-1})$ resembles the slope of the terrestrial planet hosts $(-1.2 \pm 0.4 \times 10^{-4} \text{ dex K}^{-1})$. This is unsurprising as it has been shown that most Sun-like stars likely host smaller planets (Petigura et al. 2013). Similarly, the slopes for giant planet hosts and close-in giant planet hosts are almost exactly the same. This also make sense as there is a large overlap between the close-in giant planet and giant planet populations in our sample. Astrophysically, close-in giant planets could be from the same giant planet population but have just undergone type II migration (Dawson & Johnson 2018). However, we find that all the slopes are indistinguishable within the 1σ errors. These slopes are also on the same order of magnitude as those reported in Bedell et al. (2018). We also measure slopes for each individual star compared to the Sun and find that the Sun is relatively refractory depleted compared to 87% of our solar-analog population (compared to Bedell's 80%). This suggests that there is not a significant correlation between refractory enrichment or depletion and our current knowledge of planet host status; the Sun remains relatively refractory depleted compared to all types of planet hosts.

Table 2
Test-set-inferred Labels

Column	Format	Units	Example	Description		
Identifier:						
DR3id	integer	•••	711643129958302592 Gaia DR3 ID			
Coordinates:						
ra	float	degrees	134.765818	R.A.		
dec	float	degrees	30.568571	Decl.		
TheCannon-inferred Labels:						
teff	integer	K	5915	$T_{\rm eff}$ inferred label		
teff_err	integer	K	55	$T_{\rm eff}$ inferred label error		
logg	float	dex	4.31	$\log g$ inferred label		
logg_err	float	dex	0.08	$\log g$ inferred label error		
Fe_H_	float	dex	-0.01	[Fe/H] inferred label		
Fe_H_err	float	dex	0.03	[Fe/H] inferred label error		
Mg_H_	float	dex	-0.02	[Mg/H] inferred label		
Mg_H_err	float	dex	0.04	[Mg/H] inferred label error		
C_H_	float	dex	-0.008	[C/H] inferred label		
C_H_err	float	dex	0.05	[C/H] inferred label error		
N_H_	float	dex	0.007	[N/H] inferred label		
N_H_err	float	dex	0.12	[N/H] inferred label error		
O_H_	float	dex	0.05	[O/H] inferred label		
O_H_err	float	dex	0.07	[O/H] inferred label error		
Na_H_	float	dex	-0.07	[Na/H] inferred label		
Na_H_err	float	dex	0.08	[Na/H] inferred label error		
Mn_H_	float	dex	-0.1	[Mn/H] inferred label		
Mn_H_err	float	dex	0.09	[Mn/H] inferred label error		
Cr_H_	float	dex	-0.03	[Cr/H] inferred label		
Cr_H_err	float	dex	0.04	[Cr/H] inferred label error		
Si_H_	float	dex	-0.005	[Si/H] inferred label		
Si_H_err	float	dex	0.03	[Si/H] inferred label error		
Ni_H_	float	dex	-0.04	[Ni/H] inferred label		
Ni_H_err	float	dex	0.03	[Ni/H] inferred label error		
V_H_	float	dex	-0.05	[V/H] inferred label		
V_H_err	float	dex	0.05	[V/H] inferred label error		
Ca_H_	float	dex	0.005	[Ca/H] inferred label		
Ca_H_err	float	dex	0.05	[Ca/H] inferred label error		
Ti_H_	float	dex	0.008	[Ti/H] inferred label		
Ti_H_err	float	dex	0.04	[Ti/H] inferred label error		
Al_H_	float	dex	-0.05	[Al/H] inferred label		
Al_H_err	float	dex	0.05	[Al/H] inferred label error		
Y_H_	float	dex	0.02 [Y/H] inferred label			
Y_H_err	float	dex	0.07	[Y/H] inferred label error		
Other:						
age	float	Gyr	5.84	Derived age from isoclassify		
age_err	float	Gyr	2.67	Derived error in age from isoclassify		
planet?	integer		0	Does star host planet(s)? $N = 0$, $Y = 1$		

Note. The complete table is available in the online journal. Values have been truncated in this table preview to remain concise. [N/H] was inferred using partial labels in the training step.

(This table is available in its entirety in machine-readable form.)

4.2.2. Abundance Differences between Planet Host Populations

Though the mean differences in abundances among the different types of planet hosts and the entire test set are already small, we investigate these differences further. We compare close-in giant planet hosts, giant planet hosts, and terrestrial planet hosts to the nonplanet hosts (the other 17,362 in the test set). We show the mean differences in abundances between the planet hosts and nonplanet hosts ($\Delta[X]$) in the top right panel of Figure 10. The terrestrial planet hosts are consistent in abundance space with the nonplanet hosts. The close-in giant and giant planet hosts differ from the nonplanet hosts, although no abundance has a $>4\sigma$ difference. We also compare the mean

differences for five fundamental stellar parameters, age, $T_{\rm eff}$, $\log g$, [Fe/H], and [Mg/Fe] as the representative [α /Fe] element (from [Mg/H] – [Fe/H]). The results are shown in the top left panel. The nonplanet hosts are consistent within 2σ for $T_{\rm eff}$, $\log g$, [Fe/H], and [Mg/Fe] to terrestrial planet hosts; there is a $>3\sigma$ offset of 0.01 dex in age. There are offsets $>3\sigma$ of 0.04–0.05 dex in $\log g$ and 0.06 dex in [Fe/H] for close-in giant and giant planet hosts, respectively. This raises the possibility that any differences in abundances between nonplanet hosts and planet hosts could be driven by systematic population differences in age, $\log g$, and [Fe/H] rather than intrinsic abundance differences from planet architectures. We

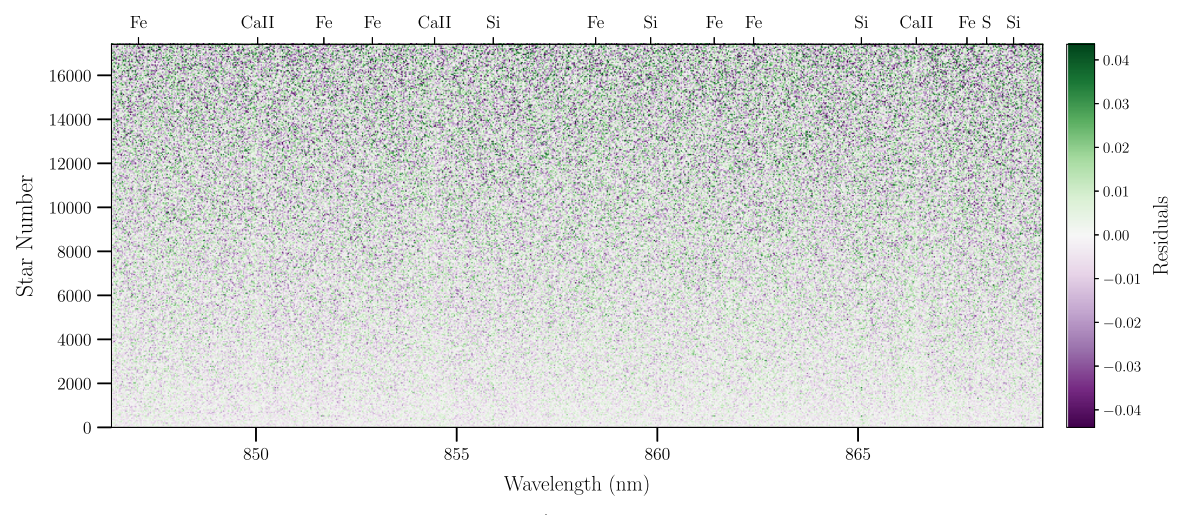


Figure 7. Residuals of the test set ordered from lowest (bottom) to highest S/N (top). The Ca triplet is remarkably well modeled. All other residuals appear stochastic in nature.

Element	$\sigma_{\rm cval} ({\rm dex})$	$\overline{\sigma_{\mathrm{lit}}}$ (dex)	$\sigma_{\rm int} ({ m dex})$
Fe	0.036	0.026	0.025
Mg	0.042	0.032	0.026
C	0.051	0.035	0.037
N	0.119	0.086	0.082
O	0.067	0.054	0.041
Na	0.076	0.04	0.064
Mn	0.089	0.034	0.082
Cr	0.04	0.023	0.033
Si	0.032	0.023	0.023
Ni	0.036	0.021	0.03
V	0.053	0.041	0.034
Ca	0.045	0.027	0.036
Ti	0.036	0.026	0.025
Al	0.05	0.045	0.023
Y	0.066	0.042	0.051

subsequently test and see this is the case, using a doppelganger comparison test.

We define doppelgangers to be stars that have the same fundamental parameters (at 1σ) as our test objects (Behmard et al. 2023; Sayeed et al. 2024), in labels of age, $T_{\rm eff}$, $\log g$, [Fe/H], and [Mg/Fe]. This enables us to build a control sample to examine any differences in elemental abundances alone at otherwise fixed conditions of evolutionary state (age, $T_{\rm eff}$, and log g) and fiducial supernova enrichment levels represented with Fe and [Mg/Fe]. For each close-in giant, giant, and terrestrial planet host, we find their associated doppelgangers in age, $T_{\rm eff}$, $\log g$, [Fe/H], and [Mg/Fe] within 1σ from the nonplanet host sample. We calculate the mean stellar parameter and abundance differences between each planet host minus their N randomly drawn doppelgangers. This gives us a representative distribution of the difference in each planet host and the doppelganger population. In the second row of Figure 10, we show the mean of these mean differences and standard error of this mean. The mean differences in stellar parameters

(left bottom panel) between the populations are of course zero since we are only comparing planet hosts to their doppelgangers. However, now we see that this in turn makes all previous nonzero abundance differences seen for planet hosts, particularly the close-in giant and giant planet hosts, consistent with zero within at most 2σ . The mean difference for [N/H] is still nonzero post–doppelganger correction, but recall this abundance was poorly labeled during the training step. The trend toward zero difference between populations agrees with those presented in Behmard et al. (2023), who also found a subset of planet hosts from the Kepler mission that are chemically indistinguishable from their doppelgangers.

We also inspect how other stellar parameters change for planet hosts when solely conditioning on T_{eff} and $\log g$. We find that there are differences in age, [Fe/H], and [Mg/Fe] that reflect the overall abundance differences from star-forming conditions as reflected by supernova elements. We then iteratively condition on the three stellar parameters that did have systematic differences (age, log g, and [Fe/H]) one at a time for all of the planet host populations. We find that conditioning on [Fe/H] has the largest impact on decreasing the abundance differences. This makes sense given the well-known planet-metallicity correlation (Fischer & Valenti 2005). In fact, we recover this exact finding in that the (close-in) giant planet hosts are on average more metal rich than the nonplanet and terrestrial planet hosts, which was causing the significant nonzero abundance differences in the top right panel of Figure 10. Conditioning on age and $\log g$ also decreases the spread in abundance differences albeit at respectively smaller scales. Thus, conditioning on all fundamental stellar parameters simultaneously results in the greatest decrease in abundance differences.

5. Discussion

In this work, we use TheCannon to train a linear model on 34 solar-analog Gaia RVS stars with high-precision literature stellar parameters and abundances, measured from high-resolution data (R > 30,000), to infer $T_{\rm eff}$, $\log g$, and 15 individual abundances ([X/H]) for 17,412 other Gaia RVS ($R \approx 11,000$) stars, 50 of which are (candidate) planet hosts. This data-driven analysis yields average upper limit precisions of 61 K in $T_{\rm eff}$, 0.09 dex in $\log g$, and 0.04–0.1 dex in [X/H] (see Table 2). These are an improvement compared to the RVS

 $[\]overline{^{10}}$ Because every planet host does not have the same number of doppelgangers, N is determined by the star with the fewest doppelgangers. This star will be compared to all of its doppelgangers, while other stars will be compared to a subset of their doppelgangers of size N.

Table 4
Planet (Candidate) Parameters from Berger et al. (2023) and the Exoplanet Archive for Planet Hosts in the Test Set

DR3	Host ID	R.A.	Decl.	Planet ID	Radius (R_{\oplus})	Orbital Period (days)
749676822006222464	tic85293053	156.8377	34.39095	toi1772.01	2.325	8.051
749676822006222464	tic85293053	156.8377	34.39095	toi1772.02	4.493	•••
6258810550587404672	HD 137496	231.74206	-16.50901	HD 137496 b	1.31	1.621
6258810550587404672	HD 137496	231.74206	-16.50901	HD 137496 c	12.6	479.9
5500031730804862720	tic350931281	90.71014	-55.53292	toi4403.01	3.097	4.462
4648587831980764160	tic141412823	84.23719	-75.61142	toi4421.01	2.964	21.701
4716158250340258944	HD 10180	24.47311	-60.51149	HD 10180 c	3.68	5.76
4716158250340258944	HD 10180	24.47311	-60.51149	HD 10180 d	3.45	16.357
4716158250340258944	HD 10180	24.47311	-60.51149	HD 10180 e	5.39	49.748
4716158250340258944	HD 10180	24.47311	-60.51149	HD 10180 f	5.24	122.744
4716158250340258944	HD 10180	24.47311	-60.51149	HD 10180 g	4.91	604.67
4716158250340258944	HD 10180	24.47311	-60.51149	HD 10180 h	9.4	2205.0
4729324799004633472	tic197807043	53.46724	-57.62129	toi2423.01	14.837	•••
4666490423895957376	tic388106759	62.854	-69.47488	toi810.01	2.32	28.306
4666490423895957376	tic388106759	62.854	-69.47488	toi810.02	2.414	90.849
4666498154837086208	tic25155310	63.37473	-69.22659	toi114.01	9.459	3.289
6411016151376518144	tic403135192	333.55961	-59.56832	toi2226.01	3.636	0.902
1433586454781584896	tic224596152	254.5033	57.30526	toi1734.01	2.435	28.874
4903786336207800576	tic281781375	12.97603	-59.34367	toi204.01	2.391	43.828
4910452812646300544	tic206541859	18.04853	-56.92538	toi4406.01	10.706	30.082
636363799347569408	epic211945201	136.5742	19.40205	epic211945201.01	6.106	19.492
636363799347569408	epic211945201	136.5742	19.40205	epic211945201.01	6.206	19.492
2581918597853527424	epic220621788	12.77001	9.51677	epic220621788.01	2.378	13.682
2079613685738988800	kic8176564	295.43967	44.03901	K02720.01	1.256	6.572
5710154317045164416	tic1003831	130.29515	-16.03633	toi564.01	7.363	1.651
5762607889340459008	tic149845414	135.5458	-3.42082	toi2545.01	2.274	7.994
3486043573401367168	tic98957720	181.0008	-28.32535	toi3501.01	18.622	15.349
4822523493384074496	tic167661160	79.70936	-36.03769	toi2479.01	3.073	36.838
4655671573080397056	tic231077395	67.65781	-70.35491	toi2238.01	2.147	3.39
4743138925656526976	tic201793781	34.68431	-54.85972	toi248.01	2.208	5.991
4762694805108531840	tic382045742	79.32368	-59.06839	toi3355.01	2.215	15.66
1602005522755589760	tic224313733	234.09914	57.89074	toi1856.01	12.396	39.402
1630906044157332224	tic307958020	256.8431	62.47554	toi4633.01	3.002	543.878
5054967123443063936	tic142868621	50.94274	-31.2652	toi2446.01	4.184	18.686
3604866386264961792	epic212357477	202.01618	-15.93798	epic212357477.01	2.236	6.327
3616931735377523712	K2-292	205.37587	-9.94607	K2-292 b	2.63	16.984
6239702034929248512	K2-287	233.07434	-22.35835	K2-287 b	9.494	14.893
2534280057557160704	epic220207374	20.992	0.25935	epic220207374.01	1.608	8.268
5820908638718592256	tic361711730	243.88501	-69.2171	toi5027.01	10.983	10.244
2104104723128736128	kic6266866	284.59168	41.63933	K05254.01	0.832 2.744	232.916
6385929006882225024 4964562700427198720	tic405425498 tic138727432	337.51776 32.91429	-67.85014 -37.89299	toi2227.01 toi853.01	16.464	4.222 6.865
	tic124573851	158.9007		toi669.01	2.559	3.945
3777506754255516800 3778075717162985600	tic169226822	160.55877	-5.18136 -3.835	toi675.01	14.399	3.943 4.178
6173451477191225984	tic271168962	210.19357	-30.58361	toi828.01	13.582	5.322
4813630986935633152	tic13883872				2.267	13.419
5260585074966996864	tic141770198	73.74111 91.8755	-41.34421 -76.69058	toi4322.01 toi4555.01	2.192	522.627
5262245367587966208	tic142087638	98.44214	-74.1901	toi2404.01	3.924	20.363
5262245367587966208	tic142087638	98.44214	-74.1901 -74.1901	toi2404.01 toi2404.02	8.978	74.605
5262245367587966208	tic142087638	98.44214	-74.1901 -74.1901	toi2404.02 toi2404.03	6.941	746.066
3406687485600728192	epic247098361	73.7668	18.65432	epic247098361.01	9.945	11.169
6266769537305193856	epic250106132	236.44605	-14.20768	epic250106132.01	3.496	22.122
6283723285046532864	tic46096489	214.68301	-14.20768 -20.27544	toi818.01	12.719	3.119
	tic43647325	76.08189				3.162
3211188618762023424 2506859165273343488	tic4364/325 tic332715376		-6.22978	toi423.01	14.788 2.724	
4617735638779366016		32.67117	-0.67888	toi4354.01		10.631 20.073
	tic318608749	9.12614	-83.56707	toi1100.01	4.138	
45456357610673408	epic210550063	61.13186	16.21665 75.64656	epic210550063.01	2.643	2.166
6357524189130820992	tic317060587	337.51024	-75.64656	toi1052.01	2.434 2.527	9.14 8.608
4866555051425383424	tic77253676	69.70423	-36.68132	toi697.01		
4870809920906672384	tic170729775	67.98437 70.99759	-34.45554 31.00664	toi2449.01	11.682 10.005	16.654
4877544322252002048	tic1167538	/0.99/39	-31.90664	toi2447.01	10.005	•••

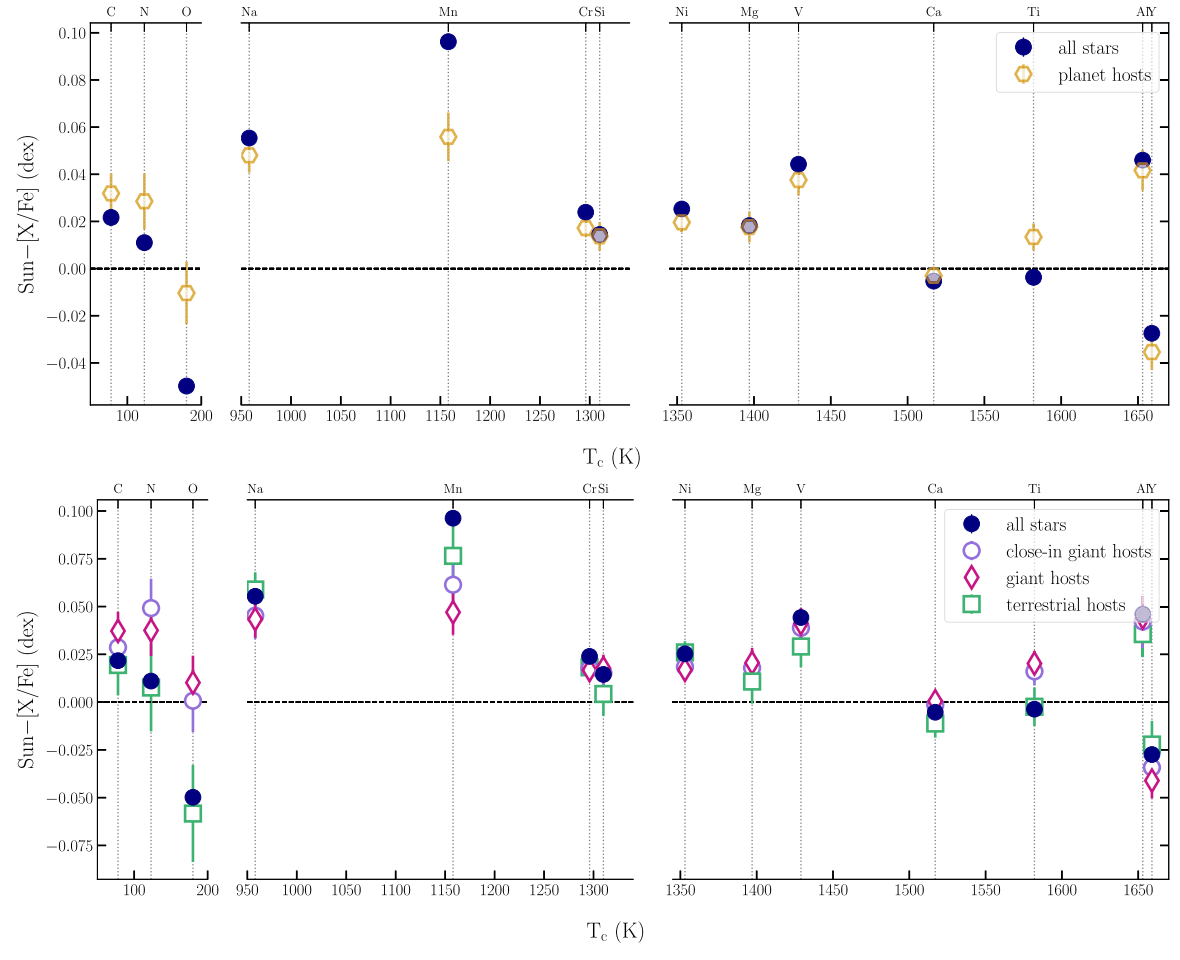


Figure 8. Mean abundance measurements of our sample with standard errors of the means (standard deviation divided by the square root of the number of stars) as a function of condensation temperature compared to the Sun. Top: all test set solar analogs appear as as navy filled circles and identified planet hosts as orange hexagons. The Sun appears relatively refractory depleted with increasing condensation temperature compared to these samples replicating Bedell et al. (2018), and the solar analogs and planet hosts are chemically indistinguishable within $2-3\sigma$. Bottom: all test set solar analogs are shown as navy filled circles, close-in giant planet hosts as purple unfilled circles, giant planet hosts as pink unfilled diamonds, and terrestrial/small planet hosts as green unfilled squares. The Sun still appears relatively depleted compared to these four samples, which are still chemically indistinguishable within $2-3\sigma$.

measurement precisions, which are 70 K for $T_{\rm eff}$, 0.11 dex for log g, and 0.15 dex for [Fe/H] compared to 0.036 dex from our results shown in Table 3.

In compiling the reference set, we used data from five different survey efforts (Bensby et al. 2014; Hinkel et al. 2014; Brewer et al. 2016; Bedell et al. 2018; Brewer & Fischer 2018). Our model works remarkably well despite typically seen offsets in literature labels due to different instruments and analysis methods used across these surveys. We see this in our initial crossvalidation test described in Section 3.1.1. That is, when treating each star in the reference set itself as a test star and applying the model trained without that star, we can recover the literature element abundance values to precisions of 0.05 ± 0.02 dex (Figure 3). The Cannon also uses the inferred labels to generate model spectra that we can compare to the observed RVS spectra. We show an example spectrum from the cross-validation in Figure 5 and a summary of the residuals (data – model) of the The Cannon-generated spectra and the RVS spectra for the test set in Figure 7. Residuals are on average <1%.

5.1. The Limits of Gaia RVS-inferred Abundances

An important consideration when using data-driven methods for low- to medium-resolution surveys is what precision can be obtained. High-resolution spectrographs are advantageous for spectroscopy due to the high-precision measurements achieved. However, we are able to obtain surprisingly high precision at much lower resolution (Ting et al. 2017). Achieving high precision is relevant in the context of the abundance dimensionality. It appears that the dimensionality of the abundance space is low, and the many abundances we infer can be well predicted using age, T_{eff} , $\log g$, and a small subset of elements. We find even just two element measurements ([Mg/H] and [Mg/Fe] or [Fe/H] and [Mg/Fe]) are enough to predict the other elements, similar to Griffith et al. (2021). The intrinsic information in the elements beyond what information is captured in T_{eff} , $\log g$, [Fe/H], [Mg/Fe], and age requires higher resolution and more precise observations to access, if such information is present. We find we do not have the precision to measure any intrinsic scatter in the majority of the other 13 elements we derive when using our five-label model to predict these abundances. Using just two labels, we can predict abundances to >87%, even after adjusting our error estimates from TheCannon to account for the input reference label errors. Measuring potential and significant differences in abundances due to planet architectures therefore requires precisions higher than what we achieve (≤ 0.02 dex), because we need to access information beyond what is already captured

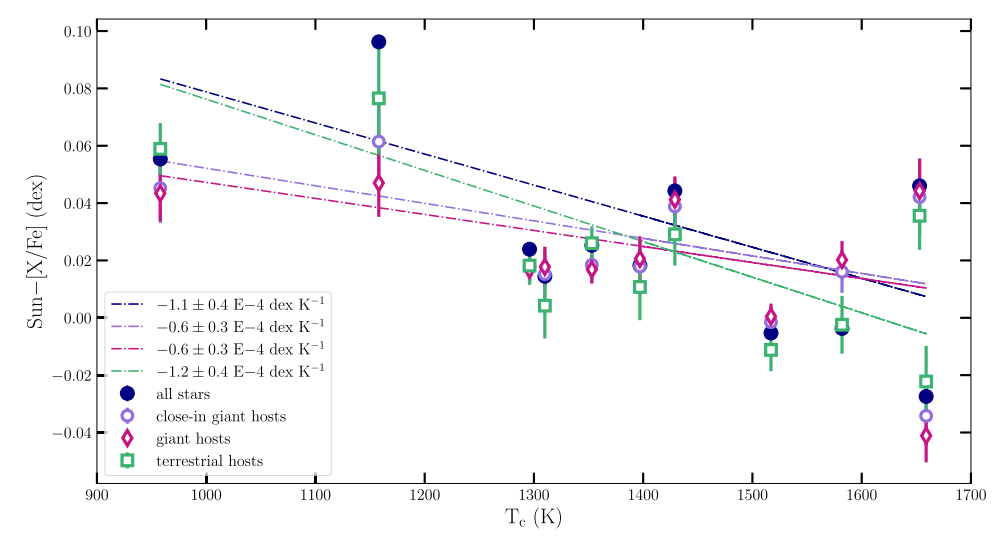


Figure 9. Linear fits of test set solar analogs (navy filled circles), close-in giant planet hosts (purple unfilled circles), giant planet hosts (pink unfilled diamonds), and terrestrial/small planet hosts (green squares) for element mean abundances and respective standard errors of the means from Na (958 K) to Y (1659 K). The slopes are indistinguishable within the errors, suggesting the increased relative depletion with condensation temperature of the Sun is unrelated to our current knowledge of planet host status.

in the 2–5 labels. Additionally, the impact of time-variable stellar atmospheres and surface motions may add complexity to measuring accurate and precise abundances at this level (Spina et al. 2020). This level of measurement precision for element abundances is more readily achievable with Gaia RVS spectra of $S/N \gtrsim 200$ (see Figure 4 of Ting et al. 2017), which only include 2% of our current sample though this can be reached in future data releases after spectra are coadded with multiple visits. This precision is certainly more accessible with high-resolution spectroscopy (R > 100,000).

While we have 44 stars in our test set with the same abundances and stellar parameters as the Sun within their errors, we have not necessarily found 44 solar birth siblings. The prospect of finding stellar birth siblings, which presumably have identical abundances, also requires this extremely high precision, and it may also be out of reach even at abundance precisions ~ 0.02 dex (e.g., Ness et al. 2018). Using the potential differentiating power of abundances also requires measuring elements from multiple nucleosynthetic families (e.g., Freeman & Bland-Hawthorn 2002; Manea et al. 2023).

We infer [X/H] for the majority of the elements. Bedell et al. (2018) and Adibekyan et al. (2016) discuss the merits of using [X/Fe] versus [X/H], which we consider here. [X/Fe] represents the enhancement or depletion of a given element from the norm of stars for a given bulk metallicity, [Fe/H], and can mitigate trends related to Galactic chemical evolution compared to [X/H]. [X/H] represents the elemental abundance with respect to the production of elements in the Big Bang. We choose to use [X/H] as the most direct transfer of labels from the training set. We test how well TheCannon performs using [X/Fe] versus [X/H] and find that TheCannon has a poorer performance and a higher bias for many labels.

It is also important to recognize the differences between abundance inferences and physical abundance measurements. In particular, C, O, Na, V, Al, and Y absorption lines are not present in the RVS wavelength region, which would typically prevent measurements of these elements in a traditional abundance analysis. However, TheCannon can use other lines to infer abundances for these elements (see the coefficients in the Appendix). Additionally, some elements

such as O produce variations across the entire spectrum due to electron donorship (e.g., Ting et al. 2018), so in a number of cases it is appropriate to use the full spectrum to infer an element, not simply the specific absorption lines.

5.2. The Sun Remains Relatively Refractory Depleted

Our finding that the element abundances between the populations of identified planet hosts and other solar-analog stars are indistinguishable can be used to help interpret the Sun's relative refractory depletion. The Sun has been shown to be relatively depleted in refractory elements with increased condensation temperature compared to 80% of other Sun-like stars (Bedell et al. 2018). In our work, we also find this trend holds true for the Sun compared to 87% of our solar-analog test set regardless of planet host status (Figures 8 and 9). The same trend holds true for the 382 most solar-like stars in our test set with the same age, $T_{\rm eff}$, $\log g$, $[{\rm Fe}/{\rm H}]$, and $[\alpha/{\rm Fe}]$ as the Sun within their errors. Thus, the source of this apparent refractory depletion trend in the Sun remains an open question.

Early work such as Meléndez et al. (2009) and Ramírez et al. (2009) suggest that refractory depletion trends can change depending on planet host type. More specifically stars like the Sun, with terrestrial planets, show this trend because terrestrial planets lock up the refractories. Such planet hosts will appear refractory depleted compared to those hosting close-in giant planets. This suggestion has been challenged by the modeling work of Kunitomo et al. (2018) who show >16 M_{\oplus} of refractoryrich material, far exceeding that of the terrestrial planets, is needed to make up the deficit seen in the Sun. Our work also challenges this theory empirically given that we see, regardless of the type of planet host, the Sun still remains relatively refractory depleted with increasing condensation temperature in comparison. What was likely being seen in Meléndez et al. (2009) and Ramírez et al. (2009) were small but systematic differences in the fundamental stellar parameters among the identified planethosting populations that propagated to abundance differences rather than intrinsic abundance differences.

Our results, given the precision limits, are inconsistent with the theory suggested by Booth & Owen (2020). They posit that

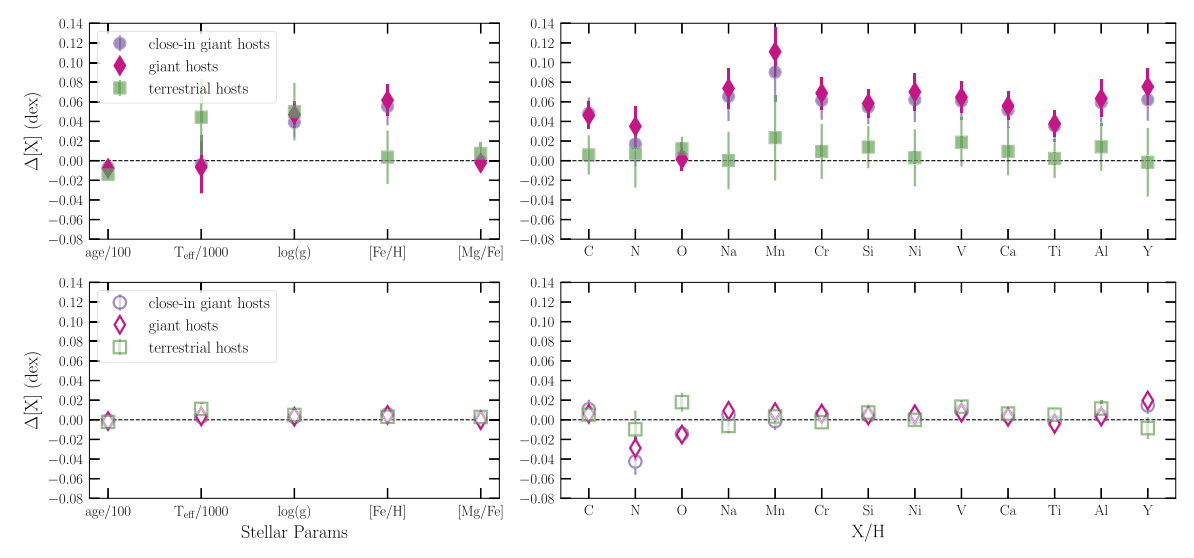


Figure 10. Mean label differences between close-in giant planet hosts (purple circles), giant planet hosts (pink diamonds), and terrestrial/small planet hosts (green squares) and nonplanet hosts. Top: there are differences in the five fundamental parameters (left) that could describe the differences seen in abundance space on the right, though no nonzero differences are more than 4σ . The error on the mean is the rms sum of the standard deviation of planet hosts divided by the square root of the number of planet hosts plus the standard deviation of test set stars divided by the square root of the number of test set stars. Bottom: the five fundamental parameters have been "doppelganger corrected" (left). All identified planet hosts are compared solely against nonplanet hosts with the same age, $T_{\rm eff}$, $\log g$, [Fe/H], and [Mg/Fe] within the errors. This decreases the spread in nonzero differences even further to $<2\sigma$. Error bars are the standard error of the mean.

giant planets, like Jupiter, could create dust traps that sequester refractory-rich dust and prevent it from falling into the host star. This has been suggested as an explanation for the abundance differences and measured refractory depletion trend of $\approx 5 \times 10^{-5}$ dex K⁻¹ in the wide binary system HD196067– HD196068 (Flores et al. 2024), which is similar to the slope we measure for giant planet hosts $(6 \times 10^{-5} \text{ dex K}^{-1}, \text{ Figure 9})$. However, we see in the top panel of Figure 10 that giant planet hosts (close in or not) are chemically indistinguishable within the errors from stars that are not known giant planet hosts. Hühn & Bitsch (2023) recently calculated that abundance differences due to dust traps from giant planets are ≈ 0.01 dex. So while giant planets could sequester elements, it is not happening at a precision we are necessarily able to detect. The solar analogs in this work do appear enriched compared to the Sun at scales larger than those shown in Hühn & Bitsch (2023) across all planet host types. Thus, the source of the Sun's refractory depletion seems to not only be from the planets it currently hosts (if it is at all).

There are obvious biases in our planet sample due to detection incompleteness. This is particularly true for objects with smaller radii and long periods in spite of the close-in giant planets in our sample having plausibly experienced type II migration from the outer part of their disks. We present these results with this caveat and do not outright refute any theories of planets suppressing refractories. Rather, we show there is no significant link between planet host status and stellar refractory composition emerging based on our current observations.

From our work, we calculate that the Sun is in the 13th percentile of the solar-analog abundance pattern distribution. The planet hosts we study are likely sampled from this abundance distribution. We confirm this is true by randomly drawing 43 stars from our test set that are not the 43 identified planet hosts 100 times. We measure the slope of their mean refractory abundances as a function condensation temperature and find an average slope of $-1.1 \pm 0.2 \times 10^{-4}$ dex K⁻¹. This is in agreement with the results from our linear fits shown in Figure 9. This indicates that the Sun is indeed a bit lower in the

general Sun-like star abundance pattern distribution but is still reasonably part of a continuous distribution. Therefore, the refractory element trends may not actually require any special explanations.

5.3. Prospects for Exoplanet Composition and Formation Studies

This catalog is a demonstration of the utility of data-driven learning in the era of big data surveys. There are certainly limits to the precision and dimensionality of Gaia RVS data. However, we have been able to infer abundances for 17,412 stars and 50 planet (candidate) hosts using a reference set made up of stars from different high-resolution spectroscopic surveys.

Host star abundances can play a role in constraining exoplanet compositions and formation pathways. While the compositions of planets can span a wider range than that of their host stars (Plotnykov & Valencia 2020), rocky planets have been shown to mirror the [Fe/Mg] and [Si/Mg] ratios of their host stars. In our own solar system, Earth and Mars have [Fe/Mg] and [Si/Mg] ratios that match the Sun's to within 10% (Unterborn & Panero 2019). Rodríguez Martínez et al. 2023 finds this is true of K2-106 b, and Adibekyan et al. (2021) generally finds a strong correlation (although not 1:1) between planet iron mass fraction and host star composition. This underscores the importance of refractory elements in rocky planet structure. We infer abundances for Si, Fe, Mg, and nine other refractory elements. Abundance measurements of volatile elements like C and O, which we also infer, are also useful as they can trace the formation and migration of planets using the various molecular ice lines present in the protoplanetary disk (Öberg et al. 2011). In order to differentiate between planet populations among stars, Hinkel & Unterborn (2018) calculate that precisions of 0.01 dex for [Si/H] and 0.02 for [Fe/H] are needed. The precision only increases for other elements. Our average upper limit precisions for Si and Fe are 0.04 dex. These precisions improve to 0.02 and 0.03 dex if we account for input reference label errors. While this entire catalog may not be used to infer or differentiate between planet compositions just as yet, we have used these data to understand the extent of the Sun's apparent refractory depletion compared to >17,000 solar analogs. With near all sky surveys like Gaia, data-driven methods like TheCannon, and increased future exoplanet discoveries from the upcoming Plato Mission (Rauer et al. 2014) and the Nancy Grace Roman Space Telescope (Spergel et al. 2015), we can assess such abundance and stellar parameter trends for stars hosting planets on a much larger and more robust scale.

Acknowledgments

We thank the anonymous referee for the extremely quick turnaround and constructive comments that helped us improve the manuscript. We thank the THYME Collaboration, Em Boudreaux, and Aylin Garcia Soto for helpful discussions. R.R. thanks the LSSTC Data Science Fellowship Program, which is funded by LSSTC, NSF Cybertraining Grant #1829740, the Brinson Foundation, and the Moore Foundation; her participation in the program has benefited this work. R.R. was supported

by NSF Graduate Research Fellowship (DGE-2236868). G.H.E. was supported by NSF Award #2102591.

This work has made use of data from the European Space Agency (ESA) mission Gaia (https://www.cosmos.esa.int/gaia), processed by the Gaia Data Processing and Analysis Consortium (DPAC; https://www.cosmos.esa.int/web/gaia/dpac/consortium). Funding for the DPAC has been provided by national institutions, in particular the institutions participating in the Gaia Multilateral Agreement. This research has made use of the NASA Exoplanet Archive, which is operated by the California Institute of Technology, under contract with the National Aeronautics and Space Administration under the Exoplanet Exploration Program.

Facilities: Gaia, Exoplanet Archive.

Software: astropy (Astropy Collaboration et al. 2013, 2018), sklearn (Pedregosa et al. 2011), scipy (Virtanen et al. 2020), TheCannon (Ness et al. 2015), Korg (Wheeler et al. 2023, 2024), numpy (Harris et al. 2020), pandas (McKinney 2010; pandas Development Team 2020), topcat (Taylor 2005), isoclassify (Huber et al. 2017; Berger et al. 2020), matplotlib (Hunter 2007), and bayestar19 (Green et al. 2019).

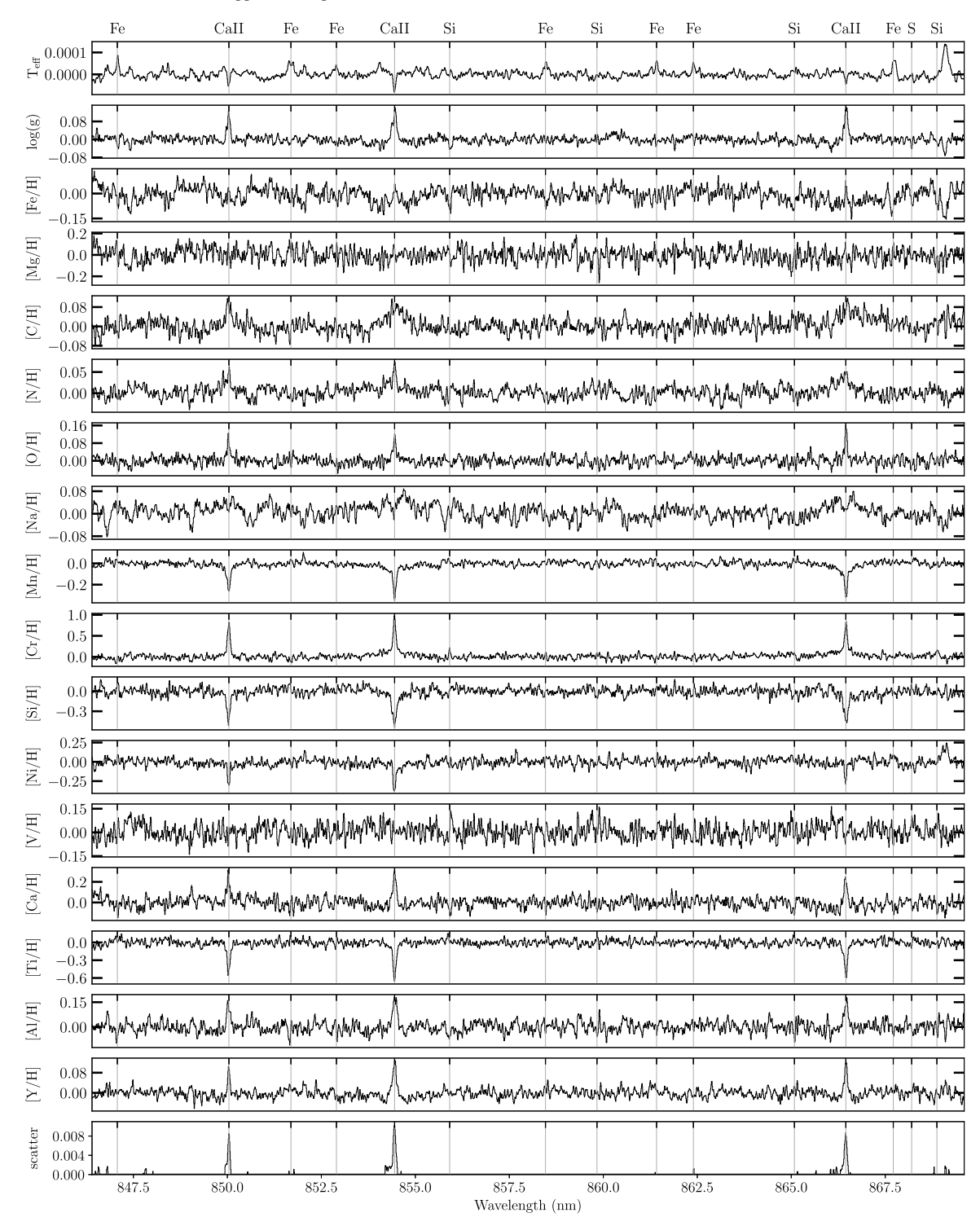


Figure A1. Coefficients of TheCannon model for each label. Most labels are best "learned" from the variance in the cores and wings of the Ca II lines, which is consistent with Rampalli et al. (2021).

Appendix Model Coefficients

In Figure A1, we show the coefficients of the TheCannon model for each label.

ORCID iDs

 Elisabeth R. Newton https://orcid.org/0000-0003-4150-841X Megan Bedell https://orcid.org/0000-0001-9907-7742

References

Adibekyan, V., Delgado-Mena, E., Figueira, P., et al. 2016, A&A, 592, A87 Adibekyan, V., Dorn, C., Sousa, S. G., et al. 2021, Sci, 374, 330 Andretta, V., Busà, I., Gomez, M. T., & Terranegra, L. 2005, A&A, 430, 669 Astropy Collaboration, Price-Whelan, A. M., Sipőcz, B. M., et al. 2018, AJ, 156, 123

```
Astropy Collaboration, Robitaille, T. P., Tollerud, E. J., et al. 2013, A&A,
   558, A33
Bedell, M., Bean, J. L., Meléndez, J., et al. 2018, ApJ, 865, 68
Behmard, A., Ness, M. K., Cunningham, E. C., & Bedell, M. 2023, AJ,
   165, 178
Bensby, T., Feltzing, S., & Oey, M. S. 2014, A&A, 562, A71
Berger, T. A., Huber, D., van Saders, J. L., et al. 2020, AJ, 159, 280
Berger, T. A., Schlieder, J. E., & Huber, D. 2023, arXiv:2301.11338
Berke, D. A., Murphy, M. T., Flynn, C., & Liu, F. 2023, MNRAS, 519, 1221
Birky, J., Hogg, D. W., Mann, A. W., & Burgasser, A. 2020, ApJ, 892, 31
Booth, R. A., & Owen, J. E. 2020, MNRAS, 493, 5079
Brewer, J. M., & Fischer, D. A. 2018, ApJS, 237, 38
Brewer, J. M., Fischer, D. A., Valenti, J. A., & Piskunov, N. 2016, ApJS,
Buchhave, L. A., Bizzarro, M., Latham, D. W., et al. 2014, Natur, 509, 593
Casey, A. R., Hawkins, K., Hogg, D. W., et al. 2017, ApJ, 840, 59
Choi, J., Dotter, A., Conroy, C., et al. 2016, ApJ, 823, 102
Cropper, M., Katz, D., Sartoretti, P., et al. 2018, A&A, 616, A5
Dawson, R. I., & Johnson, J. A. 2018, ARA&A, 56, 175
Dotter, A. 2016, ApJS, 222, 8
Fischer, D. A., & Valenti, J. 2005, ApJ, 622, 1102
Flores, M., Yana Galarza, J., Miquelarena, P., et al. 2024, MNRAS, 527, 10016
Freeman, K., & Bland-Hawthorn, J. 2002, ARA&A, 40, 487
Gaia Collaboration, Prusti, T., de Bruijne, J. H. J., et al. 2016, A&A, 595, A1
Gaia Collaboration, Vallenari, A., Brown, A. G. A., et al. 2023, A&A, 674, A1
Green, G. M., Schlafly, E., Zucker, C., Speagle, J. S., & Finkbeiner, D. 2019,
Griffith, E., Weinberg, D. H., Johnson, J. A., et al. 2021, ApJ, 909, 77
Harris, C. R., Millman, K. J., van der Walt, S. J., et al. 2020, Natur, 585, 357
Hinkel, N. R., Timmes, F. X., Young, P. A., Pagano, M. D., & Turnbull, M. C.
   2014, AJ, 148, 54
Hinkel, N. R., & Unterborn, C. T. 2018, ApJ, 853, 83
Ho, A. Y. Q., Ness, M. K., Hogg, D. W., et al. 2017, ApJ, 836, 5
Hogg, D. W., Eilers, A.-C., & Rix, H.-W. 2019, AJ, 158, 147
Huber, D., Zinn, J., Bojsen-Hansen, M., et al. 2017, ApJ, 844, 102
Hühn, L. A., & Bitsch, B. 2023, A&A, 676, A87
Hunter, J. D. 2007, CSE, 9, 90
Kunitomo, M., Guillot, T., Ida, S., & Takeuchi, T. 2018, A&A, 618, A132
Lodders, K. 2003, ApJ, 591, 1220
Magic, Z., Collet, R., Hayek, W., & Asplund, M. 2013, A&A, 560, A8
Manea, C., Hawkins, K., Ness, M. K., et al. 2023, arXiv:2310.15257
Martin, J., Fuhrmeister, B., Mittag, M., et al. 2017, A&A, 605, A113
Mayor, M., Pepe, F., Queloz, D., et al. 2003, Msngr, 114, 20
McKinney, W. 2010, in Proc. 9th Python in Science Conf., ed.
  S. van der Walt & J. Millman (Austin, TX: SciPy), 56
Meléndez, J., Asplund, M., Gustafsson, B., & Yong, D. 2009, ApJL, 704, L66
Mulders, G. D., Pascucci, I., Apai, D., & Ciesla, F. J. 2018, AJ, 156, 24
```

```
NASA Exoplanet Archive 2023, Planetary Systems, Version: 2023-08-07,
  NExScI-Caltech/IPAC, doi:10.26133/NEA12
Ness, M., Hogg, D. W., Rix, H. W., Ho, A. Y. Q., & Zasowski, G. 2015, ApJ,
  808, 16
Ness, M., Rix, H.-W., Hogg, D. W., et al. 2018, ApJ, 853, 198
Ness, M. K., Wheeler, A. J., McKinnon, K., et al. 2022, ApJ, 926, 144
Öberg, K. I., Murray-Clay, R., & Bergin, E. A. 2011, ApJL, 743, L16
pandas Development Team 2020, pandas-dev/pandas: Pandas v1.2.2, Zenodo,
  doi:10.5281/zenodo.3509134
Paxton, B., Bildsten, L., Dotter, A., et al. 2011, ApJS, 192, 3
Paxton, B., Cantiello, M., Arras, P., et al. 2013, ApJS, 208, 4
Paxton, B., Marchant, P., Schwab, J., et al. 2015, ApJS, 220, 15
Pedregosa, F., Varoquaux, G., Gramfort, A., et al. 2011, JMLR, 12, 2825
Petigura, E. A., Howard, A. W., & Marcy, G. W. 2013, PNAS, 110, 19273
Petigura, E. A., Marcy, G. W., Winn, J. N., et al. 2018, AJ, 155, 89
Plotnykov, M., & Valencia, D. 2020, MNRAS, 499, 932
Price-Jones, N., & Bovy, J. 2018, MNRAS, 475, 1410
Prša, A., Harmanec, P., Torres, G., et al. 2016, AJ, 152, 41
Ramírez, I., Meléndez, J., & Asplund, M. 2009, A&A, 508, L17
Rampalli, R., Ness, M., & Wylie, S. 2021, ApJ, 921, 78
Rauer, H., Catala, C., Aerts, C., et al. 2014, ExA, 38, 249
Recio-Blanco, A., de Laverny, P., Allende Prieto, C., et al. 2016, A&A,
  585, A93
Recio-Blanco, A., de Laverny, P., Palicio, P. A., et al. 2023, A&A, 674, A29
Rodríguez Martínez, R., Gaudi, B. S., Schulze, J. G., et al. 2023, AJ, 165, 97
Sayeed, M., Ness, M. K., Montet, B. T., et al. 2024, ApJ, 964, 42
Serenelli, A., Johnson, J., Huber, D., et al. 2017, ApJS, 233, 23
Spergel, D., Gehrels, N., Baltay, C., et al. 2015, arXiv:1503.03757
Spina, L., Nordlander, T., Casey, A. R., et al. 2020, ApJ, 895, 52
Taylor, M. B. 2005, in ASP Conf. Ser. 347, Astronomical Data Analysis
  Software and Systems XIV, ed. P. Shopbell, M. Britton, & R. Ebert
  (San Francisco, CA: ASP), 29
Ting, Y.-S., Conroy, C., Rix, H.-W., & Cargile, P. 2017, ApJ, 843, 32
Ting, Y.-S., Conroy, C., Rix, H.-W., & Asplund, M. 2018, ApJ, 860, 159
Ting, Y.-S., Freeman, K. C., Kobayashi, C., De Silva, G. M., &
  Bland-Hawthorn, J. 2012, MNRAS, 421, 1231
Ting, Y.-S., & Weinberg, D. H. 2022, ApJ, 927, 209
Unterborn, C. T., & Panero, W. R. 2019, JGRE, 124, 1704
Virtanen, P., Gommers, R., Oliphant, T. E., et al. 2020, NatMe, 17, 261
Walsen, K., Jofré, P., Buder, S., et al. 2024, MNRAS, 529, 2946
Wheeler, A., Ness, M., Buder, S., et al. 2020, ApJ, 898, 58
Wheeler, A. J., Abruzzo, M. W., Casey, A. R., & Ness, M. K. 2023, AJ,
  165, 68
Wheeler, A. J., Casey, A. R., & Abruzzo, M. W. 2024, AJ, 167, 83
Wilson, R. F., Cañas, C. I., Majewski, S. R., et al. 2022, AJ, 163, 128
Wylie, S. M., Gerhard, O. E., Ness, M. K., et al. 2021, A&A, 653, A143
Zink, J. K., Christiansen, J. L., & Hansen, B. M. S. 2019, MNRAS, 483, 4479
```